



HAL
open science

Interactions of Anti-Inflammatory and Antibiotic Drugs at Mineral Surfaces Can Control Environmental Fate and Transport

Tao Luo, Jing Xu, Wei Cheng, Lian Zhou, Remi Marsac, Feng Wu,
Jean-François Boily, Khalil Hanna

► **To cite this version:**

Tao Luo, Jing Xu, Wei Cheng, Lian Zhou, Remi Marsac, et al.. Interactions of Anti-Inflammatory and Antibiotic Drugs at Mineral Surfaces Can Control Environmental Fate and Transport. *Environmental Science and Technology*, 2022, 56 (4), pp.2378-2385. 10.1021/acs.est.1c06449 . insu-03485178

HAL Id: insu-03485178

<https://insu.hal.science/insu-03485178>

Submitted on 17 Dec 2021

HAL is a multi-disciplinary open access archive for the deposit and dissemination of scientific research documents, whether they are published or not. The documents may come from teaching and research institutions in France or abroad, or from public or private research centers.

L'archive ouverte pluridisciplinaire **HAL**, est destinée au dépôt et à la diffusion de documents scientifiques de niveau recherche, publiés ou non, émanant des établissements d'enseignement et de recherche français ou étrangers, des laboratoires publics ou privés.

1 **Interactions of anti-inflammatory and antibiotic drugs at mineral**
2 **surfaces can control environmental fate and transport**

3
4
5 Tao Luo^a, Jing Xu^b, Wei Cheng^c, Lian Zhou^a, Rémi Marsac^d, Feng Wu^e, Jean-François
6 Boily^f, Khalil Hanna ^{a,g,*}

7
8 ^a Univ Rennes, Ecole Nationale Supérieure de Chimie de Rennes, CNRS, ISCR-UMR
9 6226, F-35000, Rennes, France.

10
11 ^b State Key Laboratory of Water Resources and Hydropower Engineering Science,
12 Wuhan University, Wuhan 430072, P. R. China

13
14 ^c College of Resources and Environmental Science, South-Central University for
15 Nationalities, Wuhan 430074, P. R. China

16
17 ^d Univ Rennes, CNRS, Géosciences Rennes – UMR 6118, F-35000 Rennes, France.

18
19 ^e Hubei Key Lab of Biomass Resource Chemistry and Environmental Biotechnology,
20 School of Resources and Environmental Science, Wuhan University, Wuhan, 430079,
21 P. R. China.

22
23 ^fDepartment of Chemistry, Umeå University, Umeå, SE-901 87, Sweden

24
25 ^gInstitut Universitaire de France (IUF), MESRI, 1 rue Descartes, 75231 Paris, France.

26
27
28 *Corresponding author: Tel.: +33 2 23 23 80 27, khalil.hanna@ensc-rennes.fr

36 **Abstract**

37 Various pharmaceutical compounds often coexist in contaminated soils, yet little
38 is known about how their interactions impact their mobility. We here show that two
39 typical antibiotic and anti-inflammatory agents (nalidixic acid (NA) and niflumic acid
40 (NFA)) commonly form dimers at several representative soil- and sediment-binding
41 minerals of contrasting composition and structure. Co-binding occurs in the form of a
42 NFA-NA dimer stabilized by hydrogen bonding and van der Waals interactions. Using
43 dynamic column experiments containing goethite-coated sand, we then demonstrated
44 that pre-sorbed NA effectively captured the otherwise weakly-binding NFA from
45 solution. Simultaneously injecting NA and NFA to pre-sorbed NA enhanced even
46 further both NA and NFA loadings, thereby altering their transport under flow-through
47 conditions. We also showed that environmental level amounts of natural organic
48 matter can reduce the overall retention in column experiments, yet it does not
49 suppress dimer formation. These environmentally relevant scenarios can be predicted
50 using a new transport model that accounts for kinetics and co-binding reactions of
51 NFA onto NA bound to goethite through metal bonded, hydrogen-bonded and an
52 outer-sphere complexes. These findings have important implications on assessing the
53 fate of co-existing pharmaceutical compounds under dynamic flow conditions in
54 contaminated soils.

55

56 **Keywords:** pharmaceutical compounds; mobility; cooperative binding; transport;
57 modeling.

58

59

Synopsis

60

61 This work contributes to efforts aiming to accurately assess co-binding mechanisms

62 and the fate of co-existing contaminants in the environment.

63

64

65

66

Graphical Abstract



67

68

69

70

71 **1. Introduction**

72 Pharmaceutical and personal care products often co-exist in aquatic systems at
73 levels as high as several hundred ng per L¹⁻⁴. Recently, antibacterial and
74 anti-inflammatory agents have emerged as aqueous micropollutants in surface waters,
75 groundwaters and soils^{2,5}. The transport and mobility of these emerging contaminants
76 in the environment are strongly related to the nature and relative abundance of the
77 mineral phases (*e.g.* metal oxides and clays) commonly found in the Earth's
78 near-surface environment⁶⁻⁸. For this reason, several studies have focused on
79 interactions of organic compounds with metal-oxyhydroxides and clays⁸⁻¹². Still,
80 much remains to be learned on their fate and transport mechanisms in oxide-rich
81 environments, and particularly in multicomponent systems. In such systems,
82 adsorption, through competitive or synergistic interactions at mineral surfaces, is key
83 to determine the fate of pollutant mixtures¹³⁻¹⁵.

84

85 Recent spectroscopic, chromatographic and theoretical investigations have
86 improved the description of quinolones and fluoroquinolones adsorption to Fe-oxides
87 by identifying ligands that are (i) metal-bonded (MB; inner-sphere (IS)), (ii)
88 hydrogen-bonded (HB; direct H-bond to surface (hydr)oxo group) or (iii) bound as
89 outer-sphere (OS; separated by at least one hydration sheath) species. The relative
90 importance of these species is affected by pH, ionic strength, as well as mineral
91 surface and ligand structures¹⁶⁻¹⁹. More particularly, we have shown that the spatial

92 disposition functional groups of niflumic acid (NFA, a non-steroidal
93 anti-inflammatory) favor HB over MB species at goethite (α -FeOOH) surfaces over a
94 broad range of pH values^{18,19}. In contrast, the keto group and carboxylate groups of
95 nalidixic acid (NA, a quinolone antibiotic) favor MB species.^{19,20} Here, MB species
96 dominate under acidic conditions, while HB/OS coexists under circumneutral to
97 alkaline conditions.

98
99 Because most traditional environmental models are based on a single/individual
100 contaminant basis, little is known on their transport in mixture contaminant systems,
101 and underlying reaction mechanisms remain elusive. In addition, much of the
102 knowledge that currently exists concerns the reactivity of environmental mineral
103 surfaces in suspensions or slurry systems, and under equilibrium conditions^{7,10,21–23}.
104 Fewer investigations have been performed on the impact of water flow on the
105 interfacial processes, and much less in flow-through system where non-equilibrium
106 prevails. Moreover, non-equilibrium sorption under dynamic flow conditions is
107 particularly relevant when competitive or cooperative process in presence or
108 absence of natural organic matter (NOM) concurrently impact the mobility of target
109 compounds^{4,24,25}.

110
111 In this work, we assessed the ability of NA and NFA to co-bind at minerals
112 surfaces. To identify the mineralogical controls on NA and NFA co-binding we
113 monitored their uptake by batch adsorption on seven nanominerals of contrasting

114 composition and structure (goethite, magnetite, hematite, gibbsite, kaolinite, bentonite
115 and titanium dioxide). These natural constituents of soils and sediments are the most
116 reactive minerals in the environment, and play an important role in controlling the fate,
117 mobility and toxicity of contaminants. Then, to emulate contaminant migration in
118 natural environments, such as in aquifers and sediments, we monitored NA and NFA
119 transport in column experiments using goethite-coated quartz sand particles. Goethite,
120 a widespread mineral in aquatic and terrestrial systems, is one of the most
121 thermodynamically stable iron oxide with a high surface area²⁶. Furthermore, goethite
122 is often forming coatings on less soluble soil particles such as silica sand, and thus
123 goethite-coated sand material is generally used as a structurally stable and
124 hydraulically conductive porous medium to mimic natural mineral assemblages^{27,28}.

125 We compared NA and NFA binding (1) in isolated *vs.* mixed systems, and (2) in
126 settings emulating stagnant *vs.* flowing groundwater containing Leonardite humic acid
127 (LHA), a representative NOM. The NOM concentration range (5-10 mg/L)
128 corresponds to the dissolved organic carbon typical of shallow groundwater, soil
129 pore waters and surface waters^{29,30}. Breakthrough curves (BTCs) of NA and NFA
130 determined under different water velocities and residence times showed that
131 co-binding of NA/NFA significantly altered the mobility of each compound. Although
132 we have used an inflow concentration of NA or NFA higher than the level amounts of
133 pharmaceuticals commonly detected in environmental systems (several hundred of ng
134 per L)¹⁻⁴, previous experimental and computational quantum findings showed that the
135 formation of NFA-NA dimer at the surface of AlO(OH) or FeO(OH), is

136 thermodynamically favorable, and can even occur for the very low concentration
137 range¹⁹. In addition, dynamic breakthrough experiments provide a high solid-to-liquid
138 ratio, *i.e.* a small volume flowing through the porous media in packed bed columns,
139 and therefore a total contaminant loading more representative of environmental
140 settings^{17,18}.

141 Multisite complexation model (MUSIC) was also established to describe the
142 co-binding results of NA and NFA onto goethite, and predictions of BTC have been
143 developed from surface complexation modeling parameters combined with a new
144 kinetics term. This chemical kinetic/transport coupling was required to accurately
145 describe the mobility of NA and NFA in the different scenarios considered in this
146 study. These efforts helped identify conditions under which drug co-binding is likely
147 to prevail in the environment, and highlight the importance of coupled flow and water
148 chemistry in controlling the mobility of pharmaceutical compounds in complex
149 environmental media.

150

151 **2. Materials and Methods**

152 **2.1 Chemicals**

153 Nalidixic acid (NA), Niflumic acid (NFA), ferric nitrate nonahydrate
154 ($\text{Fe}(\text{NO}_3)_3 \cdot 9\text{H}_2\text{O}$), sodium chloride (NaCl), sodium hydroxide (NaOH), hydrochloric
155 acid (HCl) and potassium bromide (KBr) were provided by Sigma Aldrich and were
156 of analytical grade or better, and used without further purification. All solutions were
157 prepared with ultrapure water. Leonardite Humic Acid Standard (1S104H) was

158 purchased from the International Humic Substance Society. A LHA stock solution (2
159 g/L, 1276 mg C/L) was prepared by dissolving 2 g LHA in 100 mL of 1 M NaOH,
160 then diluted to 1 L with ultrapure water. Fontainebleau quartz sand (150-300 μm) was
161 purchased from VWR Prolabo (France). Ultrapure water was used in all experiments.

162

163 **2.2 Synthesis and characterization of minerals**

164 Goethite, hematite, magnetite, gibbsite were synthesized using published
165 methods, and described in the SI. Commercial TiO_2 Millennium PC-500 (> 99% of
166 anatase), Georgia kaolinite (KGa-1) and Bentonite (Na-montmorillonite) were used as
167 received. More information about synthesis and characterization are given in the
168 Supporting information (SI).

169

170 Goethite coated sand (GCS) was obtained by mixing 500 g of Fontainebleau
171 sand with an excess of goethite (~10 g) in 1L of 10 mM NaCl solution. Before coating,
172 the quartz sand was cleaned with HCl, then with H_2O_2 , and rinsed with pure water.
173 The resulting goethite-sand suspension was adjusted to pH 5 and then shaken for 24 h.
174 After that, the coated sand was washed with ultrapure water until the runoff was clear,
175 and then it was dried in oven at 60°C for 24 h. The final GCS was stored at ambient
176 temperature. Acid digestion followed by measurements of total dissolved iron using
177 Inductively Coupled Plasma Atomic Emission Spectroscopy (ICP/AES), has
178 permitted to determine the coating degree. For GCS, we found 0.9 g goethite per 100
179 g of coated sand. Previous studies from our group^{17,20} confirmed that the coating

180 procedure did not alter the reactivity of goethite particles.

181

182 The possible dissolution of the used quartz sand was also checked in sand
183 suspensions with two solid loadings, 1 or 10 g/L, aged for one month and at various
184 equilibrium pH (4-10), in pure water or 0.01 M NaCl. In both cases were dissolved
185 silicate concentrations below the detection limits of the molybdenum blue
186 spectrophotometric method (detection limit 1 μ M) and of ICP/AES analyses (detection
187 limit 0.2 μ M)).

188

189 **2.3 Batch experiments**

190 Batch adsorption experiments were conducted in 10 mL suspensions of minerals
191 in polypropylene tubes at a wide range of pH and in 10 mM NaCl to assess the
192 NA/NFA co-binding on different types of minerals. The investigated pH range was
193 adapted for each mineral to avoid mineral dissolution at very low or high pH values.
194 All experiments were carried out under an atmosphere of N₂(g) in order to avoid
195 contributions from dissolved CO₂. Suspensions were mixed for a period of 24 h by
196 end-over-end shaking, which is largely sufficient to reach equilibrium based on
197 preliminary kinetic study¹⁸. Aliquots of the resulting suspensions were thereafter
198 sampled and filtered (0.2 μ m) for analysis. NA and NFA co-binding to goethite were
199 also investigated at pH 5 \pm 0.1 in presence of various LHA concentrations. All batch
200 adsorption experiments were performed in triplicates, with a reproducibility of 5 % for
201 NA and 7 % for NFA. Results for the LHA-free systems are in the SI only.

202 NA and NFA concentrations in the aqueous solution were determined using a
203 high performance liquid chromatography (HPLC) system. This was equipped with an
204 auto sampler (Waters 717 plus) using a C18 column (250 mm×4.6 mm i.d., 5 μm),
205 and a UV detector operating at 258 nm and 283 nm (Waters UV). The mobile phase
206 was a mixture of water/acetonitrile (60:40 v/v) containing 0.1% of formic acid. The
207 flow rate of the mobile phase was set at 1 mL/min in isocratic mode.

208

209 **2.4 Continuous flow experiments**

210 Breakthrough column experiments were conducted in a glass chromatographic
211 column (1.6 cm internal diameter). The porous bed had a length of 4.9 cm and a dry
212 mass of 15 g. After packing to a uniform bulk density (1.52 g/cm³), the column was
213 wetted upward with a background electrolyte solution (NaCl, 10 mM) at a constant
214 flow rate for at least 24 h until the column was saturated and each parameter (pH,
215 conductivity) became constant. After water saturation, 1 pore volume of 10 mM KBr
216 (with 10 mM NaCl, pH 5) was injected in between the NaCl background solution to
217 determine the flow characteristics of the porous bed. The tracer BTC was recorded by
218 ion chromatography (Fig. S1 in supporting information, SI). The classical convection
219 dispersion equation (CDE) was applied to describe the 1D transport of a non-reactive
220 solute under steady-state water flow in a saturated column (*cf.* SI for detailed
221 description of model). The fitting parameters of the bromide elution confirmed the
222 flow homogeneity and predominance of a convective regime in the column. The
223 mass balance ratios calculated based on BTCs of Br⁻ were close to 100% (Fig.

224 S1). The hydrodynamic parameters estimated includes total water
225 content θ (0.36 ± 0.005) and dispersivity λ ($242 \pm 2 \mu\text{m}$) (See SI).

226

227 After the pulse tracer experiments, four sets of column experiments were
228 performed by step-injection at the same constant flow rate of : (i) NFA/(NA+NFA):
229 injection of $10 \mu\text{M}$ of NFA first, then $10 \mu\text{M}$ NA+ $10 \mu\text{M}$ NFA when the total
230 breakthrough of NFA was achieved; (ii) NA/(NA+NFA): injection of $10 \mu\text{M}$ of NA
231 first, then $10 \mu\text{M}$ NA+ $10 \mu\text{M}$ NFA when the total breakthrough of NA was achieved,
232 (iii) (NA+NFA): simultaneous injection of $10 \mu\text{M}$ NA+ $10 \mu\text{M}$ NFA directly; (iv)
233 (NA+NFA+LHA): simultaneous injection of $10 \mu\text{M}$ NA+ $10 \mu\text{M}$ NFA + $5/10 \text{ mg/L}$
234 LHA. In all four approaches, influent solutions were prepared at $\text{pH}_{\text{in}} 5 \pm 0.1$ and
235 contained 10 mM of NaCl. Continuous on-line pH measurement was performed using
236 pre-calibrated pH flow through sensor. In addition, the pH of collected fractions was
237 often checked using a pH-meter (HI2210, HANNA[®]). The breakthrough curves
238 (BTCs) were expressed as the relative aqueous concentration of solute against the
239 number of pore volumes (V/V_p), where V_p represents the pore volume of column. The
240 adsorbed amounts of NA and NFA were determined by integrating the area above the
241 entire breakthrough curve of each compound, as previously reported^{28,31}. The mass
242 balance was further confirmed by carrying out solid-phase extraction on GCS, as
243 described in previous work³². Briefly, the solid from packed column was transferred
244 into an aqueous solution and then pH was adjusted to 11, and the suspension was
245 stirred for 1h. The average extraction recovery derived from several desorption tests

246 lied at $97.9 \pm 3.5\%$, confirming that only adsorption took place in the GCS column,
247 and that molecule breakdown by, for example, oxidation, did not occur under the
248 experimental conditions of this study. The aqueous concentrations of NA and/or NFA
249 in the outflow were determined by HPLC. In all the column experiments, the leaching
250 iron from GCS column was negligible. All experiments were conducted in duplicates,
251 and the estimated error lied at 5% for NA and NFA.

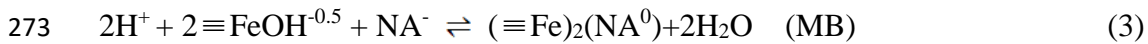
252

253 **2.5. Surface complexation modeling combined with kinetics**

254 A surface complexation model (SCM) was used to predict adsorption under
255 equilibrium condition. However, non-equilibrium may predominate in the dynamic
256 column experiments, and thus implementation of kinetics in surface complexation
257 reactions is crucial to accurately describe the mobility behavior. It was reported that a
258 fast formation of outer sphere complexes is a prerequisite for inner sphere (IS)
259 complexes formation, which is a rate-limiting process^{33,34}. According to a previous
260 spectroscopic study³⁴ showing that the conversion of hydrogen-bonded organic
261 species to MB complexes was time-dependent, HB and OS complexes can be
262 considered as intermediate species in our proposed conceptual model. To integrate
263 kinetics in our SCM, we assume surface complexation reactions occur in two steps: (i)
264 formation of precursor surface species (fast intermediate step) and (ii) formation of
265 final surface species (rate-limiting step). According to our previous spectroscopic and
266 theoretical investigations^{18,19}, NA can form (i) MB surface complexes *via* a NA keto
267 group and one oxygen of the carboxylate group, (ii) HB complexes (surface

268 hydration-shared ion pair) and (iii) OS complexes (solvent-surface
 269 hydration-separated ion pair, where NA keeps its first hydration sphere) as follows:

270



274 All modeling parameters are provided in Table S2.

275

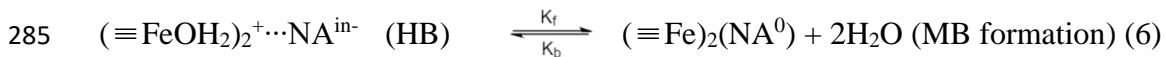
276 To distinguish the two-step reactions in PHREEQC-2, we have applied the
 277 previously published approach³⁵. Briefly, we defined one intermediate ('in') 'NAⁱⁿ'
 278 and one equilibrium 'NA' species. Here, 'NAⁱⁿ' is an intermediate complex first in the
 279 form of a OS species:



281 This OS species then converts to a HB species:



283 This conversion is a fast process, whereas the resulting HB species converts to a MB
 284 species through the following rate-limiting process:



286 Here, k_f and k_b are forward and backward rate coefficients (T^{-1}) respectively, which
 287 could be obtained by curve fitting, as previously reported.^{35,36}. Preliminary fitting
 288 procedures allowed us to set forward rate constant k_f and backward rate constant k_b to
 289 0.050 and 0.009, respectively.

290

291 The three plane model (TPM) was employed to describe the charge of the
292 goethite/water interface, which requires two capacitances for the 0- ($C_1 = 2.3 \text{ F/m}^2$)
293 and the 1-plane ($C_2 = 1.07 \text{ F/m}^2$). Then multi-site complexation (MUSIC) model and
294 PHREEQC-2 was used for modelling the species transport in the GCS-packed column.
295 Though singly ($\equiv \text{FeOH}^{-0.5}$), doubly ($\equiv \text{Fe}_2\text{OH}$) and triply ($\equiv \text{Fe}_3\text{O}^{-0.5}$ and \equiv
296 $\text{Fe}_3\text{OH}^{+0.5}$) coordinated oxygens exist at the goethite surface, we assumed that NA and
297 NFA tend to bind to reactive $\equiv \text{FeOH}^{-0.5}$ sites of goethite through HB, OS and even
298 MB (only for NA) complexes based on our studies^{18,19}. The reactive site density is
299 given as detailed in our previous work: $[\equiv \text{FeOH}^{-0.5}] = 3.12 \text{ sites/nm}^2$ and $[\equiv \text{Fe}_3\text{O}^{-0.5}] =$
300 3.12 sites/nm^2 on (001)/(101) planes (90% of the surface area), and $[\equiv \text{FeOH}^{-0.5}] = 7.4$
301 sites/nm^2 on (210)/(010) plane (10% of the surface area).

302

303 Our modeling strategy is described as follows. Surface hydrolysis and surface
304 complexation reactions including NA/NFA dimer formation were taken from our
305 previous batch sorption study¹⁸. For the column system, NA and NFA adsorption were
306 first modeled in their respective single systems. The corresponding surface
307 complexation constants were then used to predict binding in the binary system, and
308 the NA-NFA dimer formation constant was calibrated from the experimental data. The
309 column system was described by 1D transport, with p successive equal width cells (Δz
310 $= L/p$, L is the total column length, in this study $p = 20$). Solution transported between
311 p_n and p_{n+1} in time steps Δt and at the defined flow rate and dispersion through the

312 specific transport procedure implemented into PHREEQC-2. After each time step, this
313 procedure is coupled with the geochemical code for each cell³⁷. All parameters used
314 for transport modeling are provided in Table S2.

315

316 **3. Results and discussion**

317 Our previous works^{18,19} showed that enhancement in NFA binding, which is
318 otherwise considerable weaker than NA, results from the intermolecular interactions
319 with the goethite-bound NA. We ascribed this enhancement to a NFA-NA dimer
320 whose energetically favored formation (-0.5 eV compared to free molecules) is
321 predominantly driven by van der Waals interactions¹⁹. For reference, at pH 5, which
322 will be focused in our transport work, NA loadings on goethite (0.33 $\mu\text{mol}/\text{m}^2$; 0.20
323 NA/nm²) are more than 3 times larger than NFA (~ 0.10 $\mu\text{mol}/\text{m}^2$; 0.06 NFA/nm²) (Fig.
324 S2). Dimer formation in mixed NA and NFA solutions can enhance, in turn, NFA
325 loadings by a factor of ~ 2.5 ($\sim 0.10 \rightarrow \sim 0.25$ $\mu\text{mol}/\text{m}^2$) and NA loadings by ~ 1.2 (0.33
326 $\rightarrow \sim 0.40$ $\mu\text{mol}/\text{m}^2$) (Fig. S2).

327

328 Comparison of this enhancement effect with a suite of other minerals (SI) of
329 contrasting composition and structure shows that NFA binding in the binary system
330 was greatest on goethite. Namely, it followed the order: goethite (2.5-fold) > TiO₂
331 (2-fold) > magnetite (1.8-fold) > gibbsite (1.5-fold, pH 6) \approx kaolinite (1.5-fold) >
332 bentonite (1.3-fold) \approx hematite (1.3-fold). See the SI for a more detailed discussions
333 of these results where we explain that NA-NFA dimer formation is greater on

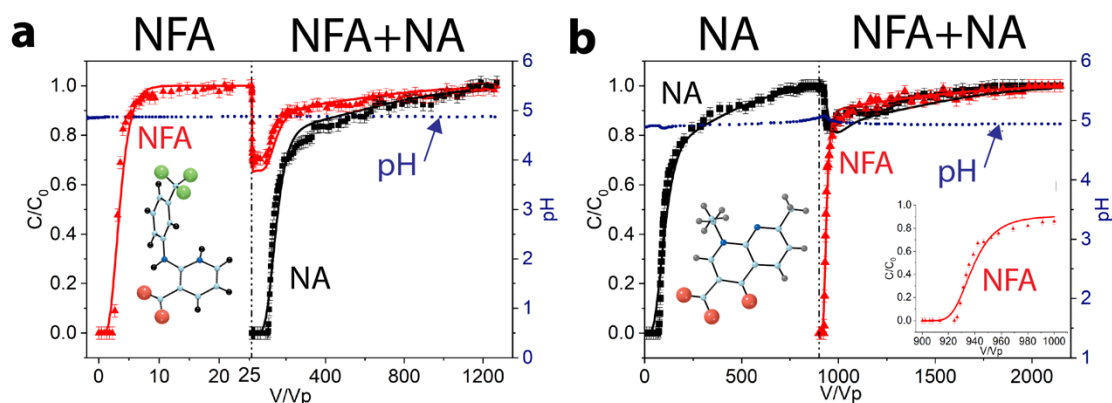
334 nanominerals typically with homogeneous distributions of reactive –OH functional
335 groups (goethite, TiO₂, magnetite), than those typically, with –OH limited to edges of
336 platy minerals with unreactive basal faces (kaolinite, bentonite, hematite). For this
337 reason, we focused our work on the effects of water flow and natural organic matter
338 on NA-NFA interactions using goethite.

339

340 **3.1. NA-NFA dimer formation under water flow**

341 To explore the propensity of NA-NFA dimer formation under flow-through
342 conditions, we performed dynamic flow experiments (Figs. 1, and 2) with columns
343 filled with goethite-coated sand (GCS). First, we find that injection of a mixed
344 solution of NA+NFA after *total breakthrough of NFA* (Fig. 1a) decreased NFA outlet
345 concentrations due to NA-NFA dimer formation on the goethite surface. This started
346 at $\sim 27 V/V_p$, reached a plateau at $\sim 29.5 V/V_p$, then it gradually increased to a
347 complete breakthrough at $\sim 1200 V/V_p$. In contrast, injecting a mixed solution of
348 NA+NFA after *total breakthrough of NA* (Fig. 1b) pushed the breakthrough point of
349 NFA to $\sim 25 V/V_p$ (insert of Fig. 1b) compared to $2.3 V/V_p$ in the single system (Fig.
350 S3). The BTC of NFA then tailed extensively before reaching a total breakthrough,
351 thus adopting a classical sigmoidal shape akin to that of NA. Here, NA loadings
352 increased from $0.68 \mu\text{mol}/\text{m}^2$ in the single system to $0.90 \mu\text{mol}/\text{m}^2$ in the binary
353 system (Fig. S4), a consequence of the pre-loaded NFA (Fig. 1). Simultaneously
354 injecting NA and NFA after total breakthrough of NA increased both NA and NFA
355 loadings ($0.90 \mu\text{mol NA}/\text{m}^2$; $0.33 \mu\text{mol NFA}/\text{m}^2$), however at levels close to the

356 values obtained where NFA was first injected (Fig. 1). As a result, we find that NA
 357 and NFA exert a mutual effect on their breakthrough behavior under flow and this is
 358 basically explained from NA-NFA dimer formation at the goethite surface.



359

360 **Figure 1.** The full range of experimental breakthrough curves of NA and NFA through
 361 GCS-packed column in two successive steps at constant flow rate (0.5 ml/min). (a)
 362 Step I: injection of 10 μ M NFA and 10 mM NaCl at $pH_{in} 5 \pm 0.1$ until the complete
 363 breakthrough of NFA. Step II: injection of mixture of 10 μ M NA + 10 μ M NFA and
 364 10 mM NaCl at $pH_{in} 5 \pm 0.1$. The solid lines represent modelling results. (b) Step I:
 365 injection of 10 μ M NA and 10 mM NaCl at $pH_{in} 5 \pm 0.1$ until the complete
 366 breakthrough of NA. Step II: injection of mixture of 10 μ M NA + 10 μ M NFA and 10
 367 mM NaCl at $pH_{in} 5 \pm 0.1$. Insert is the breakthrough curve of NFA in the initial stage.
 368 The solid lines represent modelling results.

369

370 Irrespective of the injection scenario, NA exhibits an extended tailing suggesting
 371 kinetic limitations under the experimental conditions of this study. Because all of our
 372 bromide tracer experiments (Figs. S1 and S5) were well described using the CDE
 373 model, the tailing could not be explained by physical non-equilibrium effects, water
 374 regionalization into mobile/immobile zones or diffusion limitations between two
 375 water zones^{38,39}. Moreover, the BTCs of NA and NFA in single systems were
 376 compared by normalizing the curves by their retardation factor to that of the bromide

377 tracer (Fig. S6). For NFA, the steepness of BTC showed coincidence with that of
378 bromide, and only a short tail was observed. However, the normalized BTC of NA
379 exhibits a significant difference in steepness and shape with respect to that of bromide.
380 This discrepancy suggests the occurrence of chemical kinetic limitations or
381 rate-controlled sorption processes under flow-through conditions. This is particularly
382 the case for transport of the more strongly binding NA. This was confirmed further by
383 results (Fig. S7) revealing greater NA loadings under conditions of lower flow rate
384 (0.1 mL/min) that promotes higher residence times.

385

386 To check for the occurrence of kinetic limitations, SCM modeling with or
387 without kinetics were compared for the BTC of NA (Fig. S8). These results confirmed
388 that only kinetics implemented with SCM could describe the mobility behavior. In
389 contrast, the equilibrium SCM seems sufficient for NFA, likely because of weaker and
390 faster adsorption of NFA mainly through HB and OS complexes¹⁸ (the first stage of
391 Fig. 1a). However, as NFA adsorption on goethite was strongly related to kinetically
392 limited NA adsorption, an extended tailing of NFA in the second stage was observed.
393 As only the sorption kinetics of NA were considered here, we anticipate that this
394 could affect the adsorption of NFA through co-binding reactions (*cf.* Table S2). Under
395 such conditions, our combined SCM and kinetics reproduced the mobility of both NA
396 and NFA (Fig. 1).

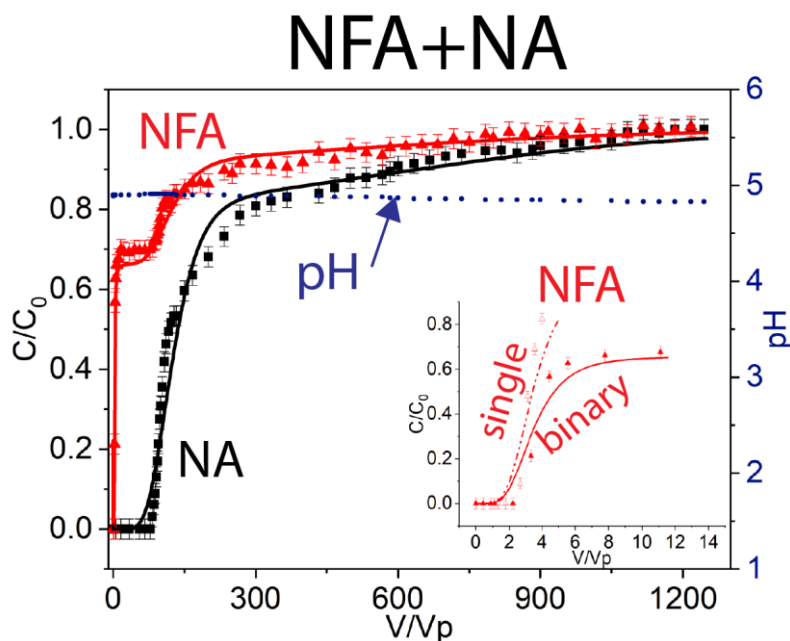
397

398 To provide further evidence for the co-dependency of NA and NFA binding to

399 GCS, we investigate the transport of the compounds under conditions where both NA
400 and NFA were injected simultaneously (Fig. 2) to a clean column. This revealed
401 two-step breakthrough behavior in the form of two fronts and of two plateaus in the
402 outlet concentration of NFA. This contrasts with the cases of where NFA was injected
403 before (Fig. 1a) or simultaneously with NA (Fig. 2). NFA sorption in the binary
404 system increased sharply to $0.34 \mu\text{mol}/\text{m}^2$, compared to that in the single system, yet,
405 they still kept the same breakthrough point at $2.3 V/V_p$ (insert of Fig. 2). In
406 conclusion, although NA and NFA adopted contrasting BTCs from different injection
407 schemes (NFA/(NFA+NA), NA/(NFA+NA), and (NFA+NA)), their surface loadings
408 after total breakthrough were largely comparable (see Table S3). Here, NA and NFA
409 loadings both increased in the binary compound systems, 1.3 times for NA and 16-19
410 times for NFA compared to the single system. As such, although NA and NFA
411 transport processes depend on the injection methodology, because of the high-affinity
412 NA to goethite, the injection order has almost no effect on NA and NFA loadings and
413 in the co-binding behavior in the binary systems.

414

415 Finally, we confirmed these co-binding effects in experiments conducted at a
416 lower flow rate ($0.1 \text{ mL}/\text{min}$; Fig. S7), where an extended tailing for NA or NFA was
417 also revealed. As a result, the same model previously used in sequential injection has
418 adequately described the behavior of NA and NFA in simultaneous injection approach
419 (Fig. 2).



421

422 **Figure 2.** Experimental and calculated breakthrough curves of NA and NFA in binary
 423 system at flow rate of 0.5 mL/min through GCS-packed column. Inflowing solution
 424 contains mixture of 10 μ M NA and 10 μ M NFA 10 and 10 mM NaCl at $\text{pH}_{\text{in}} = 5 \pm 0.1$.
 425 Insert is the breakthrough curves of NFA in the initial stage. The solid lines represent
 426 modelling results.

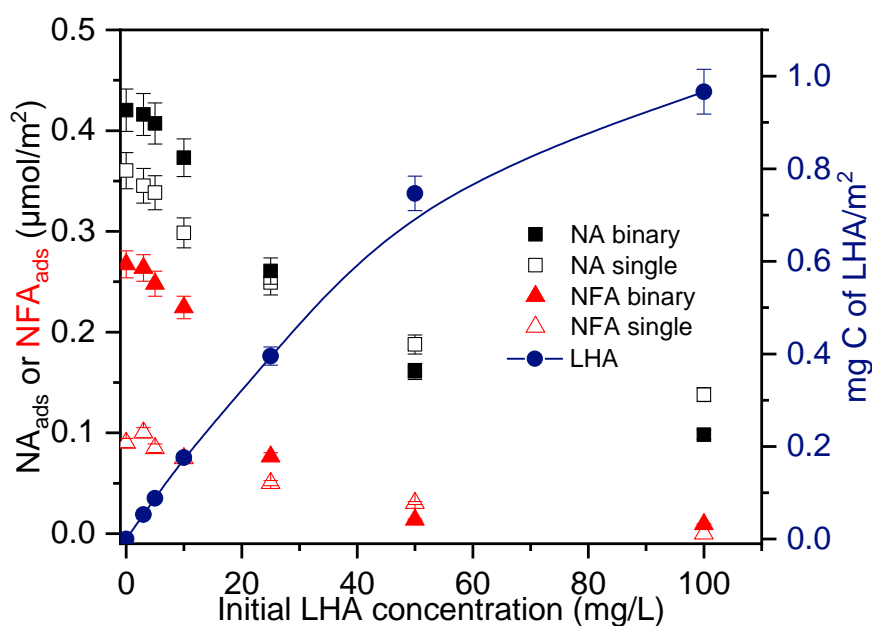
427

428 3.2 Altered fate of NA and NFA transport by natural organic matter

429 Building upon these results, we evaluated how NOM altered the fate of NA and
 430 NFA interactions. We used LHA as a representative NOM at loadings of up to ~ 1 mg
 431 C/m^2 (~ 50 C atoms/ nm^2) at pH 5 on goethite. From batch adsorption experiments
 432 (Fig. 3) we find that LHA binding effectively decreased, yet did not completely
 433 suppress, NA loadings. At the same time, we find that LHA fully suppressed NFA
 434 co-binding at LHA loadings above ~ 0.2 mg C/m^2 (~ 10 C/ nm^2). Based on previous
 435 work from our group⁴⁰, the goethite surface still exposed unreacted $-\text{OH}$ groups at
 436 this loading, and is therefore not entirely covered by LHA. Still, bound LHA was

437 sufficiently effective to prevent binding NFA to the near-interfacial region of goethite
 438 for NA/NFA dimer formation. One possible explanation is that LHA altered the
 439 interfacial hydration environment and the surface charge of goethite, and thus the
 440 potential energy landscape for the NFA diffusion across the goethite/water interface
 441 and onto goethite-bound NA. It is also interesting to note that LHA offer no
 442 possibilities for NFA binding via, for example, van der Waals π - π electron coupling
 443 interactions. The enhanced uptake of NFA with NA is therefore driven by a very
 444 specific steric control between these two molecules.

445



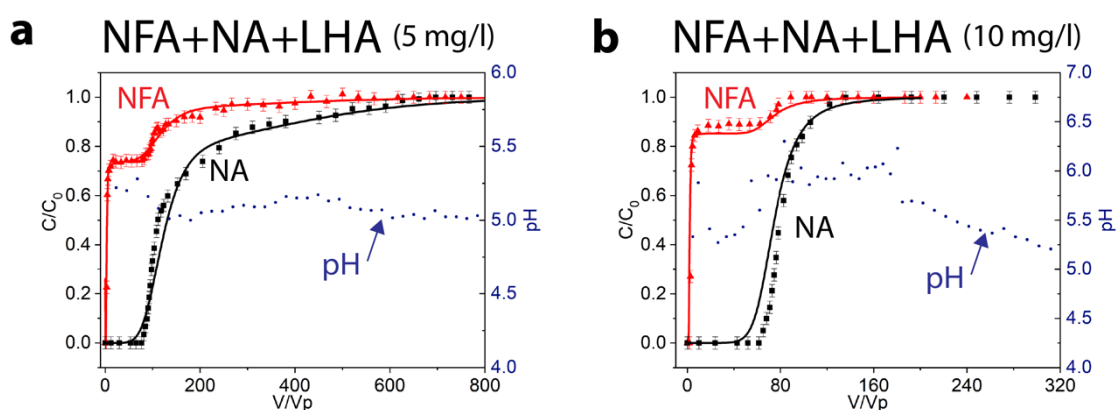
446

447 **Figure 3.** The effect of humic acid on the adsorption of NA and NFA on 0.5 g/L
 448 goethite in single ($[NA]_{tot} = 20 \mu M$ or $[NFA]_{tot} = 20 \mu M$) and binary ($[NA]_{tot} =$
 449 $[NFA]_{tot} = 20 \mu M$) system at pH 5 and ionic strength 10 mM (NaCl).

450

451 Experiments under flow (Fig. 4), again using GCS, showed that LHA at two
 452 environmentally-relevant concentrations for groundwater and surface waters^{29,30} (5
 453 and 10 mg/L) also affected NA and NFA mobility. Despite the competitive binding

454 with LHA, co-binding and a two-step breakthrough behavior were still observed (Fig.
 455 4a,b). Small breakthrough times and shorter tailing (steeper BTC) likely resulted from
 456 the consumption of adsorption sites by LHA. At relatively low LHA loadings, both
 457 NA and LHA compounds bound to goethite surface sites through ligand-exchange and
 458 hydrogen bonding, in turn altering the breakthrough behavior of NA. This competitive
 459 binding between NA and carboxylic/aromatics compounds of LHA may occur at the
 460 first step, followed probably by further adsorption of NA to LHA covered goethite.
 461 NFA enhanced adsorption could be clearly observed (from 0.02 to 0.17 $\mu\text{mol}/\text{m}^2$ at 5
 462 mg/L LHA), though this increase was reduced with increasing in LHA amount (from
 463 0.02 to 0.04 $\mu\text{mol}/\text{m}^2$ at 10 mg/L LHA), likely because of the decrease in NA sorption
 464 as a result from LHA competitive binding (*cf.* Table S3).



465

466 **Figure 4.** Experimental and calculated breakthrough curves of NA and NFA in
 467 multicomponent system with LHA at flow rate of 0.5 mL/min through GCS-packed
 468 column. a) Inflowing solution contains mixture of 10 μM NA, 10 μM NFA and 5
 469 mg/L of LHA and 10 mM NaCl at $\text{pH}_{\text{in}} = 5 \pm 0.1$. b) Inflowing solution contains
 470 mixture of 10 μM NA, 10 μM NFA and 10 mg/L of LHA and 10 mM NaCl at $\text{pH}_{\text{in}} = 5$
 471 ± 0.1 . The solid lines represent modelling results.

472

473 Based on previous studies^{20,41,42} we can expect that LHA binding results in a
474 molecular fractionation caused by selective adsorption of heterogeneous LHA
475 components. Lower molecular weight fractions of LHA with higher aromaticity could
476 have primarily, and preferentially, bound to goethite in the first adsorption stage⁴².
477 The higher molecular weight fractions, such as lignin-like and aliphatic compounds,
478 could have, in turn, bound in the following stage⁴². This view falls in line with the
479 breakthrough behavior of LHA in GCS column, particularly in terms of the
480 discrepancy between TOC and UV, which we report in Fig. S9 of the SI. In essence,
481 higher TOC values with respect to UV absorbance at 254 nm were observed during
482 the first adsorption stage. This aligns with the concept that LHA compounds of
483 smaller molecular weight were preferentially adsorbed and successively replaced
484 those of higher weight, as previously reported³⁷. The same behavior was previously
485 observed when only LHA was injected in GCS column²⁰, suggesting that the presence
486 of NA and NFA did not significantly affect the binding of LHA components in
487 column.

488

489 As NOM consists of a polydisperse mixture of organic molecules of varying
490 molecular size, incorporation of complex binding reactions of the LHA components in
491 TLM model is not straightforward. To simplify the model, we only considered sites
492 consumed by LHA components. Then we reduced the available goethite site density
493 (*i.e.* 15 % reduction for 5 mg/L LHA; 60% reduction for 10 mg/L LHA) to describe
494 the modification of NA and NFA BTC in presence of LHA. These results could

495 suggest that changes in site density were not linearly correlated to LHA loadings, and
496 this could be explained by LHA fractionation and complex interactions with goethite.
497 We have also slightly adjusted the surface NA-NFA dimer formation constant of NA
498 and NFA (Table S2) ($24.4 \rightarrow 23.8$ for 5 mg/L LHA; $24.4 \rightarrow 23$ for 10 mg/L LHA) to
499 improve the fit to the data, as the presence of LHA likely alters the formation of
500 NA-NFA dimer. Because of the functional (*e.g.* carboxylates) groups of LHA, the
501 complexation constant of NA on goethite by HB (Table S2) was also modified (20.4
502 $\rightarrow 20.6$ for 5 mg/L LHA; $20.4 \rightarrow 21$ for 10 mg/L LHA). These slight adjustments
503 improved the fit of our model to the experimental data (Fig. 4), and thus our ability to
504 predict multicomponent transport in complex systems. This consequently adds further
505 confidence to the ability of our proposed model to account for NA and NFA
506 (co)-binding under real-world conditions.

507

508 **Environmental implications for environmental fate of pollutant mixtures**

509 Emerging contaminants such as pharmaceutical compounds in the environment
510 often occur in mixtures rather than as individual entities. The increasing occurrence of
511 multiply contaminated aquatic ecosystems worldwide require efforts to predict
512 synergistic and antagonistic effects affecting the transport of toxic agents in nature.

513

514 This study contributes to mounting evidence showing that mobility of pollutant
515 mixtures cannot be predicted based on single-compound based adsorption data. More
516 particularly, we showed that mineral-bound antibiotics can be new adsorption sites for

517 other contaminants at mineral surfaces. Since this cooperative phenomenon is
518 strongly dependent on the molecular structure of target compound (*e.g.*, possibility of
519 Van der Waals interactions and/or hydrogen bonding), it cannot be generalizable to all
520 pharmaceutical compounds. Indeed, a parallel set of efforts showed that no co-binding
521 occurred with sulfamethoxazole (SMX) neither with NA nor NFA, because of the lack
522 of molecular interactions of SMX with co-existing compounds and goethite surfaces.
523 In contrast, ciprofloxacin (CIP) containing carboxyl and carbonyl functional groups,
524 enhanced NFA binding, because CIP strongly binds to goethite surfaces, and may act
525 as an attachment site for NFA. Therefore, this work raises the importance of
526 recognizing drug co-binding, and lack of co-binding, for accurately predicting the fate
527 of complex pharmaceutical mixtures in the environment.

528 Flow-through column experiments showed that co-binding caused by
529 intermolecular interactions considerably affects the mobility and transport of NA and
530 NFA in reactive porous media. These new findings combined with batch data and
531 previous theoretical calculations¹⁹ confirmed that the co-binding phenomenon takes
532 place at the mineral surface, and over a wide range of aqueous concentration. Though
533 the concentration in inflow solution may appear higher than the level of aqueous
534 concentration commonly found in aquatic systems¹⁻⁵, continuous flow-through
535 conditions offered the possibility to work with a suitable soil-aqueous phase ratio, and
536 then monitor the effects of dispersion and nonequilibrium sorption on the transport of
537 pollutants. This would certainly bring dynamic-flow tests closer to environmental and
538 real-world conditions.

539 The presence of environmental level amounts of natural organic matter can
540 reduce the overall retention by minerals, yet it does not suppress cooperative binding.
541 Taking these phenomena into account in a new SCM, which even accounts for kinetic
542 effects, allowed us to predict cooperative adsorption under dynamic flow and
543 non-equilibrium conditions. This new transport model has the potential of
544 successfully predicting the fate of pharmaceutical compounds, as NA and NFA, in
545 various different environmentally relevant scenarios, and over a wide range of
546 concentration including the level amounts commonly detected in environmental
547 systems.

548 As these co-binding mechanisms at mineral surfaces are not often considered in
549 traditional thermodynamic modeling, our findings raise the importance of recognizing
550 co-binding as a mechanism contributing to the migration of antibiotics and
551 anti-inflammatory agents in complex environmental mixtures. As such, this work
552 contributes to efforts aiming to accurately assess co-binding mechanisms at
553 environmental surfaces, and the fate of co-existing contaminants in the environment.

554

555 **Supporting Information.** Synthesis and characterization of minerals; tracer
556 experiments and modeling; co-binding of NA and NFA on different nanominerals;
557 experimental BTCs of NA or NFA with different flow rates and calculated BTCs of
558 NA by using equilibrium and kinetic model in PHREEQC-2. Breakthrough curves of
559 LHA at 5 and 10 mg/L.

560

561 **Acknowledgements**

562 This work was supported by the Institut Universitaire de France, the Swedish
563 Research Council (2020-04853), the French National Research Agency via the
564 C-FACTOR project (ANR-18-CE01-0008) and the CNRS (PICS 2018-2020). We
565 gratefully acknowledge the Chinese Scholarship Council of PR China for providing
566 financial support for Tao Luo to stay at the ENSCR.

567

568 **References**

- 569 (1) Fatta-Kassinos, D.; Meric, S.; Nikolaou, A. Pharmaceutical Residues in
570 Environmental Waters and Wastewater: Current State of Knowledge and Future
571 Research. *Anal. Bioanal. Chem.* **2011**, *399* (1), 251–275.
- 572 (2) Dębska, J.; Kot-Wasik, A.; Namieśnik, J. Fate and Analysis of Pharmaceutical
573 Residues in the Aquatic Environment. *Crit. Rev. Anal. Chem.* **2004**, *34* (1), 51–67.
- 574 (3) Heberer, T. Occurrence, Fate, and Removal of Pharmaceutical Residues in the
575 Aquatic Environment: A Review of Recent Research Data. *Toxicol. Lett.* **2002**, *131*
576 (1), 5–17.
- 577 (4) Wu, Q.; Li, Z.; Hong, H. Adsorption of the Quinolone Antibiotic Nalidixic Acid
578 onto Montmorillonite and Kaolinite. *Appl. Clay Sci.* **2013**, *74*, 66–73.
- 579 (5) Khetan, S. K.; Collins, T. J. Human Pharmaceuticals in the Aquatic Environment:
580 A Challenge to Green Chemistry. *Chem. Rev.* **2007**, *107* (6), 2319–2364.
- 581 (6) Linker, B. R.; Khatiwada, R.; Perdrial, N.; Abrell, L.; Sierra-Alvarez, R.; Field, J.
582 A.; Chorover, J. Adsorption of Novel Insensitive Munitions Compounds at Clay
583 Mineral and Metal Oxide Surfaces. *Environ. Chem.* **2015**, *12* (1), 74–84.
- 584 (7) Figueroa, R. A.; Mackay, A. A. Sorption of Oxytetracycline to Iron Oxides and
585 Iron Oxide-Rich Soils. *Environ. Sci. Technol.* **2005**, *39* (17), 6664–6671.
- 586 (8) Han, H.; Rafiq, M. K.; Zhou, T.; Xu, R.; Mašek, O.; Li, X. A Critical Review of
587 Clay-Based Composites with Enhanced Adsorption Performance for Metal and
588 Organic Pollutants. *J. Hazard. Mater.* **2019**, *369* (February), 780–796.
- 589 (9) Nayak, P. S.; Singh, B. K. Removal of Phenol from Aqueous Solutions by

590 Sorption on Low Cost Clay. *Desalination* **2007**, 207 (1–3), 71–79.

591 (10) Cheng, W.; Elaheh, Lot, K.; Remi, M.; Hanna, K. Adsorption of Quinolone
592 Antibiotics to Goethite under Seawater Conditions: Application of a Surface
593 Complexation Model. *Environ. Sci. Technol.* **2019**, 53, 1130–1138.

594 (11) Gao, J.; Pedersen, J. A. Adsorption of Sulfonamide Antimicrobial Agents to Clay
595 Minerals. *Environ. Sci. Technol.* **2005**, 39 (24), 9509–9516.

596 (12) Sheng, F.; Ling, J.; Wang, C.; Jin, X.; Gu, X.; Li, H.; Zhao, J.; Wang, Y.; Gu, C.
597 Rapid Hydrolysis of Penicillin Antibiotics Mediated by Adsorbed Zinc on Goethite
598 Surfaces. *Environ. Sci. Technol.* **2019**, 53 (18), 10705–10713.

599 (13) Gu, B.; Mehlhorn, T. L.; Liang, L.; McCarthy, J. F. Competitive Adsorption,
600 Displacement, and Transport of Organic Matter on Iron Oxide: I. Competitive
601 Adsorption. *Geochim. Cosmochim. Acta* **1996**, 60 (11), 1943–1950.

602 (14) Gu, B.; Mehlhorn, T. L.; Liang, L.; McCarthy, J. F. Competitive Adsorption ,
603 Displacement , and Transport of Organic Matter on Iron Oxide: II. Displacement and
604 Transport. *Geochim. Cosmochim. Acta* **1996**, 60 (16), 2977–2992.

605 (15) Liu, S. Cooperative Adsorption on Solid Surfaces. *J. Colloid Interface Sci.* **2015**,
606 450, 224–238.

607 (16) Evanko, C. R.; Dzombak, D. A. Surface Complexation Modeling of Organic
608 Acid Sorption to Goethite. *J. Colloid Interface Sci.* **1999**, 206, 189–206.

609 (17) Hanna, K.; Boily, J. F. Sorption of Two Naphthoic Acids to Goethite Surface
610 under Flow through Conditions. *Environ. Sci. Technol.* **2010**, 44 (23), 8863–8869.

611 (18) Xu, J.; Marsac, R.; Wei, C.; Wu, F.; Boily, J. F.; Hanna, K. Cobinding of

612 Pharmaceutical Compounds at Mineral Surfaces: Mechanistic Modeling of Binding
613 and Cobinding of Nalidixic Acid and Niflumic Acid at Goethite Surfaces. *Environ.*
614 *Sci. Technol.* **2017**, *51* (20), 11617–11624.

615 (19) Xu, J.; Marsac, R.; Costa, D.; Cheng, W.; Wu, F.; Boily, J. F.; Hanna, K.
616 Co-Binding of Pharmaceutical Compounds at Mineral Surfaces: Molecular
617 Investigations of Dimer Formation at Goethite/Water Interfaces. *Environ. Sci.*
618 *Technol.* **2017**, *51* (15), 8343–8349.

619 (20) Cheng, W.; Zhou, L.; Marsac, R.; Boily, J. F.; Hanna, K. Effects of Organic
620 Matter–Goethite Interactions on Reactive Transport of Nalidixic Acid: Column Study
621 and Modeling. *Environ. Res.* **2020**, *191*, 110187.

622 (21) Gu, C.; Karthikeyan, K. G. Sorption of the Antimicrobial Ciprofloxacin to
623 Aluminum and Iron Hydrous Oxides. *Environ. Sci. Technol.* **2005**, *39* (23),
624 9166–9173.

625 (22) Haderlein, S. B.; Weissmahr, K. W.; Schwarzenbach, R. P. Specific Adsorption
626 of Nitroaromatic Explosives and Pesticides to Clay Minerals. *Environ. Sci. Technol.*
627 **1996**, *30* (2), 612–622.

628 (23) Yang, Y.; Duan, J.; Jing, C. Molecular-Scale Study of Salicylate Adsorption and
629 Competition with Catechol at Goethite/Aqueous Solution Interface. *J. Phys. Chem. C*
630 **2013**, *117* (20), 10597–10606.

631 (24) Shakiba, S.; Hakimian, A.; Barco, L. R.; Louie, S. M. Dynamic Intermolecular
632 Interactions Control Adsorption from Mixtures of Natural Organic Matter and Protein
633 onto Titanium Dioxide Nanoparticles. *Environ. Sci. Technol.* **2018**, *52* (24),

634 14158–14165.

635 (25) Kretzschmar, R.; Robarge, W. P.; Amoozegar, A. Influence of Natural Organic
636 Matter on Colloid Transport through Saprofite. *Water Resour. Res.* **1995**, *31* (3),
637 435–445.

638 (26) Cornell, R. M.; Schwertmann, U. *The Iron Oxides: Structure, Properties,*
639 *Reactions, Occurrences and Uses*; 2003.

640 (27) Rusch, B.; Hanna, K.; Humbert, B. Coating of Quartz Silica with Iron Oxides:
641 Characterization and Surface Reactivity of Iron Coating Phases. *Colloids Surfaces A*
642 *Physicochem. Eng. Asp.* **2010**, *353* (2–3), 172–180.

643 (28) Hanna, K.; Martin, S.; Quilès, F.; Boily, J.-F. Sorption of Phthalic Acid at
644 Goethite Surfaces under Flow-Through Conditions. *Langmuir* **2014**, *30* (23),
645 6800–6807.

646 (29) McKnight, D. M.; Aiken, G. R.; Thorn, K. A.; Bencala, K. E.; Zellweger, G. W.;
647 Feder, G. L. Sorption of Dissolved Organic Carbon by Hydrous Aluminum and Iron
648 Oxides Occurring at the Confluence of Deer Creek with the Snake River, Summit
649 County, Colorado. *Environ. Sci. Technol.* **1992**, *26* (7), 1388–1396.

650 (30) Helbling, E. W.; Zagarese, H. Photochemistry of Chromophoric Dissolved
651 Organic Matter in Natural Waters. In *UV Effects in Aquatic Organisms and*
652 *Ecosystems*; 2003; 185–219.

653 (31) Pokharel, R.; Li, Q.; Zhou, L.; Hanna, K. Water Flow and Dissolved Mn(II) Alter
654 Transformation of Pipemidic Acid by Manganese Oxide. *Environ. Sci. Technol.* **2020**,
655 *54* (13), 8051–8060.

- 656 (32) Zhou, L.; Martin, S.; Cheng, W.; Lassabatere, L.; Boily, J. F.; Hanna, K. Water
657 Flow Variability Affects Adsorption and Oxidation of Ciprofloxacin onto Hematite.
658 *Environ. Sci. Technol.* **2019**, *53* (17), 10102–10109.
- 659 (33) Yiacoumi, S.; Tien, C. Modeling Adsorption of Metal Ions from Aqueous
660 Solutions. I. Reaction-Controlled Cases. *Journal of Colloid And Interface Science*.
661 1995, pp 333–346.
- 662 (34) Axe, K.; Persson, P. Time-Dependent Surface Speciation of Oxalate at the
663 Water-Boehmite (γ -AlOOH) Interface: Implications for Dissolution. *Geochim.*
664 *Cosmochim. Acta* **2001**, *65* (24), 4481–4492.
- 665 (35) Zhou, L.; Cheng, W.; Marsac, R.; Boily, J.-F.; Hanna, K. Silicate Surface
666 Coverage Controls Quinolone Transport in Saturated Porous Media. *J. Colloid*
667 *Interface Sci.* **2021**, *607*, 347-356.
- 668 (36) Nkedi-Kizza, P.; Shinde, D.; Savabi, M. R.; Ouyang, Y.; Nieves, L. Sorption
669 Kinetics and Equilibria of Organic Pesticides in Carbonatic Soils from South Florida.
670 *J. Environ. Qual.* **2006**, *35* (1), 268–276.
- 671 (37) David, L. P.; Appelo, C. A. J. User's Guide to PHREEQC (Version 2)— A
672 Computer Program for Speciation, Batch-Reaction, One-Dimensional Transport, and
673 Inverse Geochemical Calculations; 1995.
- 674 (38) Brusseau, M. L.; Gerstl, Z.; Augustijn, D.; Rao, P. S. C. Simulating Solute
675 Transport in an Aggregated Soil with the Dual-Porosity Model: Measured and
676 Optimized Parameter Values. *J. Hydrol.* **1994**, *163* (1–2), 187–193.
- 677 (39) Šimůnek, J.; van Genuchten, M. T. Modeling Nonequilibrium Flow and

678 Transport Processes Using HYDRUS. *Vadose Zo. J.* **2008**, 7 (2), 782–797.

679 (40) Cheng, W.; Hanna, K.; Boily, J. F. Water Vapor Binding on Organic
680 Matter-Coated Minerals. *Environ. Sci. Technol.* **2019**, 53 (3), 1252–1257.

681 (41) Kleber, M.; Sollins, P.; Sutton, R. A Conceptual Model of Organo-Mineral
682 Interactions in Soils: Self-Assembly of Organic Molecular Fragments into Zonal
683 Structures on Mineral Surfaces. *Biogeochemistry* **2007**, 85 (1), 9–24.

684 (42) Coward, E. K.; Ohno, T.; Sparks, D. L. Direct Evidence for Temporal Molecular
685 Fractionation of Dissolved Organic Matter at the Iron Oxyhydroxide Interface.
686 *Environ. Sci. Technol.* **2019**, 53 (2), 642–650.

687